JACS
JOURNAL OF THE AMERICAN CHEMICAL SOCIETY
pubs.acs.org/JACS
Article

Continuous Electrical Conductivity Variation in M_3(Hexaiminotriphenylene)$_2$ (M = Co, Ni, Cu) MOF Alloys

Tianyang Chen, Jin-Hu Dou, Luming Yang, Chenyue Sun, Nicole J. Libretto, Grigorii Skorupskii, Jeffrey T. Miller, and Mircea Dincă*

Cite This: J. Am. Chem. Soc. 2020, 142, 12367−12373
Read Online
ACCESS | Metrics & More | Article Recommendations | Supporting Information

ABSTRACT: We report on the continuous fine-scale tuning of band gaps over 0.4 eV and of the electrical conductivity of over 4 orders of magnitude in a series of highly crystalline binary alloys of two-dimensional electrically conducting metal−organic frameworks $M_3(HITP)_2$ (M = Co, Ni, Cu; HITP = 2,3,6,7,10,11-hexaiminotriphenylene). The isostructurality in the $M_3(HITP)_2$ series permits the direct synthesis of binary alloys $(M_xM'_{3-x})(HITP)_2$ (MM′ = CuNi, CoNi, and CoCu) with metal compositions precisely controlled by precursor ratios. We attribute the continuous tuning of both band gaps and electrical conductivity to changes in free-carrier concentrations and to subtle differences in the interlayer displacement or spacing, both of which are defined by metal substitution. The activation energy of $(Co_xNi_{3-x})(HITP)_2$ alloys scales inversely with an increasing Ni percentage, confirming thermally activated bulk transport.

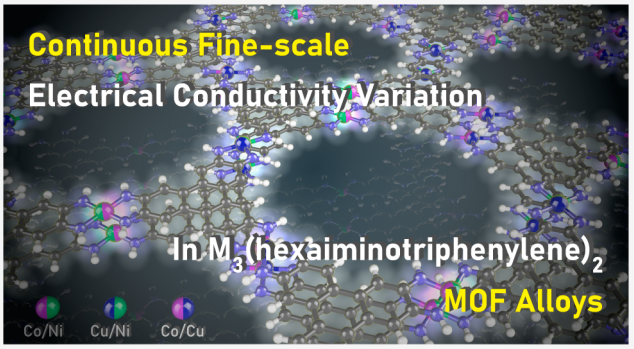

INTRODUCTION

The ability to change the electronic energy levels of the valence and conduction bands in semiconductors is one of the foundational principles of modern electronics. In principle, the same applies to electrically conducting metal−organic frameworks (MOFs), a class of emerging crystalline porous conductors.[1,2] Finely tuning their electronic properties, be it their absolute conductivity or the activation energy for charge transport, is crucial for optimizing their performance as active materials in supercapacitors,[3−5] batteries,[6] electrocatalysis,[7−11] chemiresistive sensors,[12−17] and thermoelectrics.[18,19] However, this has proven difficult in conducting MOFs, where changes in the conductivity are most often enacted by varying the structure rather than the composition. Whereas different structures indeed lead to different conductivities, structural changes rarely allow for continuous fine-tuning of electronic energy levels. Notable exceptions involve redox doping,[20] such as in tetracyanoquinodimethane-doped $Cu_3(BTC)_2$, a system that allows smooth variation of the conductivity of over 6 orders of magnitude,[21] or more commonly via I_2 doping of relatively insulating host frameworks.[17]

In inorganic semiconductors, a much more successful strategy toward band engineering is isostructural alloying, such as in $Si_{1-x}Ge_x$. We show here that one of the prototypical electrically conducting MOFs, $Ni_3(HITP)_2$ (HITP = 2,3,6,7,10,11-hexaiminotriphenylene), is amenable to similar compositional tuning. Binary alloys $(M_xM'_{3-x})(HITP)_2$ (MM′ = CuNi, CoNi, and CoCu) allow precise control over the M/M′ ratios and are isostructural with the parent compounds $M_3(HITP)_2$ (M = Co, Ni, Cu), here reported with significantly improved crystallinity compared to published procedures (see Figure 1). Alloying enables continuous variation of electrical conductivity of over 4 orders of magnitude from 5.8×10^{-3} to 55.4 S/cm.

RESULTS AND DISCUSSION

Although pure $M_3(HITP)_2$ (M = Ni, Cu, Co) have been reported with varying degrees of crystallinity and porosity,[9,12,22] systematic investigations of potential mixed-metal phases required the development of consistent synthetic procedures for high-quality crystalline and porous powders of all three MOFs. Generally, the synthesis of $M_3(HITP)_2$ involves the coordination of amino groups to metal ions, subsequent deprotonation of amino groups (typically by aqueous ammonia), and followed by oxidation in air. The absence of air prevents the formation of any precipitate (Figure S1) and air is thus considered critical. However, replacing ammonia with a weaker base, such as CH_3CO_2Na led to significant improvements in the crystallinity for $Ni_3(HITP)_2$

Received: April 29, 2020
Published: June 12, 2020

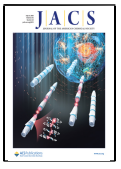

https://dx.doi.org/10.1021/jacs.0c04458
J. Am. Chem. Soc. 2020, 142, 12367−12373

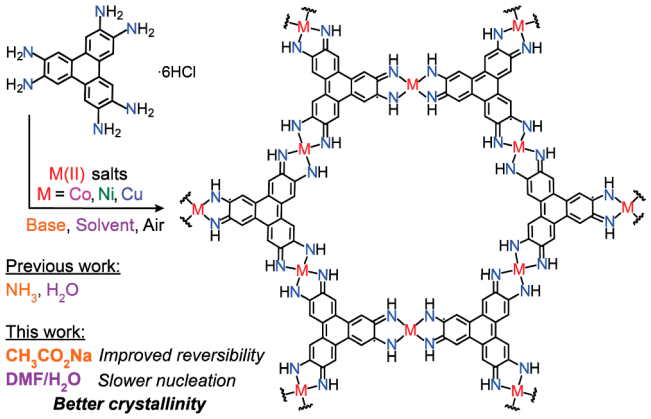

Figure 1. Synthesis of $M_3(HITP)_2$ (M = Co, Ni, Cu) and $(M_xM'_{3-x})(HITP)_2$ alloys.

and $Cu_3(HITP)_2$ (see Figures S3 and S4 and related discussions in section S3 in the Supporting Information). Most strikingly, $Co_3(HITP)_2$ crystallizes only in the presence of CH_3CO_2Na, with ammonia yielding an essentially amorphous phase (Figures S2 and S5–S7). The crystallinity of all three compounds can be further improved by employing coordinating solvents/H_2O mixtures (e.g., *N*,*N*-dimethylformamide (DMF) for $Co_3(HITP)_2$, dimethyl sulfoxide (DMSO) for $Ni_3(HITP)_2$, and *N*,*N*-dimethylacetamide (DMA) for $Cu_3(HITP)_2$). The organic cosolvents modulate the rate of deprotonation, thereby retarding nucleation,[23] and have higher donicity/donor numbers than water,[24] which affects the reversibility of the metal–ligand bond formation and further controls crystal growth.[23]

Crystallinity improvements also correlate with enhanced permanent porosity. N_2 adsorption isotherms at 77 K for $M_3(HITP)_2$ samples activated by heating at 90 °C under dynamic vacuum gave Brunauer–Emmett–Teller (BET) surface areas of 805.5 ± 0.5, 884.7 ± 0.9, and 495.4 ± 1.3 m^2/g for the Co, Ni, and Cu materials, respectively (Figure S10). These are considerably higher than previously reported values and confirm the improved synthetic procedures and material quality developed here.[9,18] Uniform pore size distributions were found in $M_3(HITP)_2$ by a pore size distribution analysis (Figure S11). A thermogravimetric analysis (TGA) revealed that $M_3(HITP)_2$ samples undergo pronounced weight losses above 200 °C, likely due to decomposition (Figure S12).

Scanning electron microscopy (SEM) revealed that black $Ni_3(HITP)_2$ and $Cu_3(HITP)_2$ powders consist of hexagonal, 1–2 μm-long rod-like crystals, whereas $Co_3(HITP)_2$ consists of polycrystalline flakes several hundreds of nanometers wide (Figures S6 and S7). Their morphology was further confirmed by low-magnification transmission electron microscopy (Figures S16–S18). All materials exhibit sufficiently high crystallinity for the Pawley refinement of their respective powder X-ray diffraction (PXRD) data (Figure 2a). Surprisingly, PXRD data for all materials gave best fits for the orthorhombic space group *Cmcm* (Figure 2a and Table S1), confirming a lower symmetry than the previously reported hexagonal systems.[12,22] The lower symmetry is also a consequence of an improved crystallinity and indicates less averaging of the stacking arrangement in the *c* direction. Indeed, the synchrotron PXRD data allows the observation of subtle differences among the three materials for both the

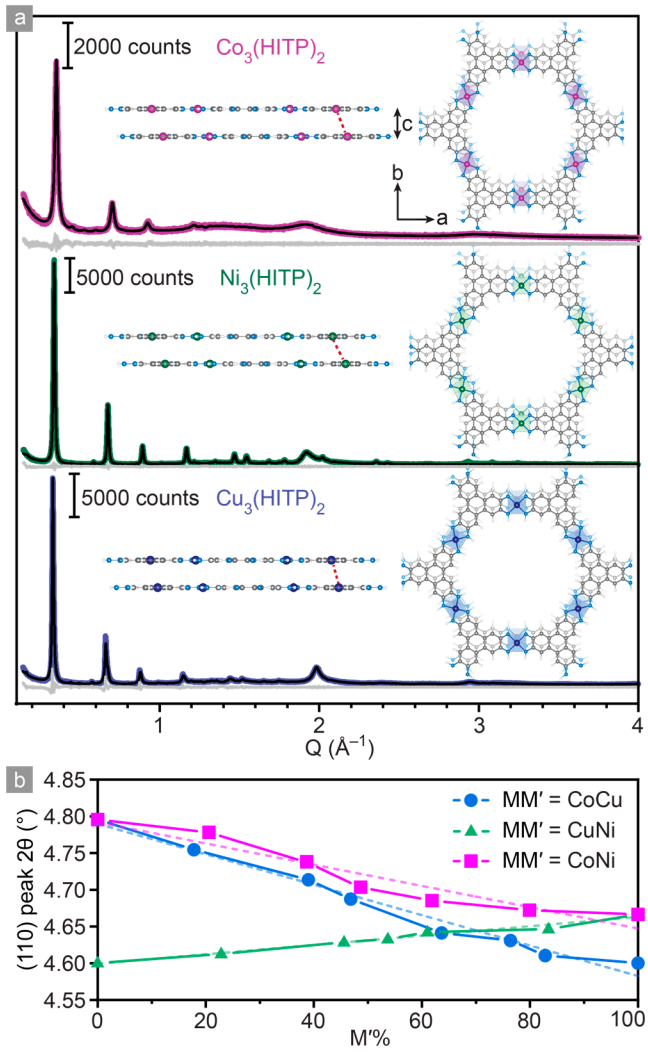

Figure 2. (a) Synchrotron PXRD patterns and corresponding Pawley refinements for $Co_3(HITP)_2$, $Ni_3(HITP)_2$, and $Cu_3(HITP)_2$. Insets show the simulated structures (both the *ab* direction and *c* direction). The red dashed lines indicate interlayer displacement. (b) Continuous changes of the crystal lattice parameters as evidenced by shifts in the (110) peak position for $(Co_x/Cu_{3-x})(HITP)_2$, $(Co_xNi_{3-x})(HITP)_2$, and $(Cu_xNi_{3-x})(HITP)_2$ alloys. Solid lines are a guide to the eye; dashed lines show the linear fit to the Vegard's law, with R^2 values of 0.98, 0.92, and 0.98, respectively.

interlayer displacement (*D*) along the *b* direction and the interlayer spacing (*S*) along the *c* direction. Thus, $Ni_3(HITP)_2$ exhibits the largest *D* value, 1.56(2) Å, whereas $Cu_3(HITP)_2$ has the smallest *S* value of only 3.16(8) Å. The latter is significantly smaller than the previously reported value, 3.30 Å, which was derived from a more poorly crystalline sample.[11] The *S* spacing is evidently connected with the strength of the interaction between the 2D sheets, which has recently been shown to contribute significantly to the electrical conductivity in layered lanthanide MOFs;[25] precise measurements of this value are important for future computations involving these materials.

Structural details from the Pawley refinements were confirmed by high-resolution transmission electron microscopy (HRTEM), with all three materials exhibiting hexagonal lattices (Figure 3). Importantly, the Fast-Fourier transform (FFT) analysis of the HRTEM micrographs provided lattice

https://dx.doi.org/10.1021/jacs.0c04458
J. Am. Chem. Soc. 2020, 142, 12367–12373

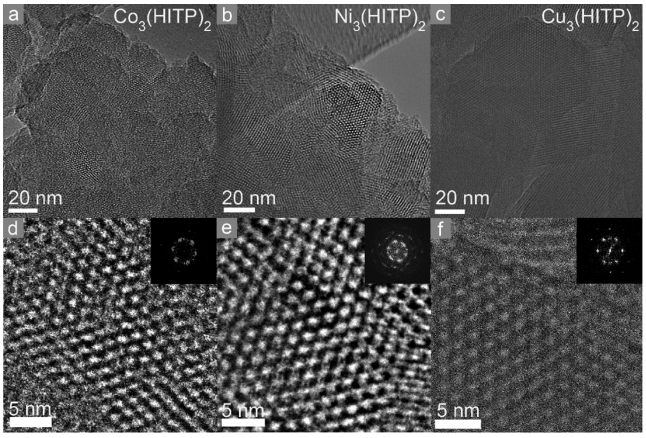

Figure 3. HRTEM images of $Co_3(HITP)_2$ (a and d), $Ni_3(HITP)_2$ (b and e), and $Cu_3(HITP)_2$ (c and f). Insets show the FFT analysis of the micrographs in (d), (e), and (f).

parameters, which are in excellent agreement with those obtained from PXRD (Tables S2–S4). HRTEM also allows precise measurements of π–π stacking distances of 3.25 Å for $Ni_3(HITP)_2$ and 3.12 Å for $Cu_3(HITP)_2$, again in excellent agreement with those obtained from the PXRD analysis (Figures S16–S18).

Owing to their nearly identical structures, $M_3(HITP)_2$ (M = Co, Ni, Cu) can be produced from binary mixtures of metal precursors with continuously variable compositions. To illustrate this, we targeted three binary series $(M_xM'_{3-x})(HITP)_2$: 5 compositions in the Cu/Ni space, 5 for Co/Ni, and 6 for Co/Cu. The final M/M′ ratios were determined by inductively coupled plasma-mass spectrometry (ICP-MS), X-ray photoelectron spectroscopy (XPS), and/or energy-dispersive X-ray spectroscopy (EDS), all of which confirmed that the final metal compositions were similar to those of the precursors (Figure S19).

A series of spectroscopic and analytical techniques confirmed the uniform composition of the MOF alloys, with $(Co_xNi_{3-x})(HITP)_2$ as a representative example. STEM elemental mapping of $(Co_xNi_{3-x})(HITP)_2$ samples revealed a uniform distribution of Co and Ni atoms within single crystallites/grains, confirming the formation of true mixed phases rather than individual particles or phase-segregated islets of $Co_3(HITP)_2$ and $Ni_3(HITP)_2$ (Figures S20–S25). Tellingly, the morphology of $(Co_xNi_{3-x})(HITP)_2$ particles also evolves gradually from nanoflakes for the cobalt-rich $(Co_{2.38}Ni_{0.62})(HITP)_2$ to nanorods for the nickel-rich $(Co_{0.60}Ni_{2.40})(HITP)_2$ (Figures S8, S9). Finally, monotonous shifts of the (110) peak position in the corresponding PXRD patterns confirm a systematic increase in the *b* unit cell parameter of $(Co_xNi_{3-x})(HITP)_2$ with increasing Ni content (Figure 2b). Similar changes are found in the $(Cu_xNi_{3-x})(HITP)_2$ and $(Co_xCu_{3-x})(HITP)_2$ series (Figures 2b and S26 and Table S5), all of which follow Vegard's law, an empirical formula describing solid solutions.[26]

XPS and X-ray absorption spectroscopy (XAS) confirmed that all metals are in the +2 formal oxidation state and exhibit square–planar coordination geometry. The XPS Co $2p_{3/2}$ peak of $Co_3(HITP)_2$ has a binding energy of 780.9 eV with a prominent satellite at 786.7 eV (Figure S29). These are consistent with Co^{2+} compounds, as satellite features rarely appear for Co^{3+} compounds.[4,27] Furthermore, $Co_3(HITP)_2$ resides in the Co(II) region in the Wagner plot[28] of Co based on the Co $2p_{3/2}$ binding energy and Co LMM kinetic energy (769.7 eV, Figure S30). The XPS spectra of $Ni_3(HITP)_2$ and $Cu_3(HITP)_2$ exhibit single Ni $2p_{3/2}$ and Cu $2p_{3/2}$ peaks at 855.2 and 933.5 eV, respectively, as expected for Ni^{2+} and Cu^{2+} (Figure S29).[29,30] The weak satellite accompanying the Ni $2p_{3/2}$ peak suggests Ni^{2+} is diamagnetic in $Ni_3(HITP)_2$.[31] The complementary Cu LMM peak with a kinetic energy of 918.2 eV also locates $Cu_3(HITP)_2$ in the Cu(II) region of the Wagner plot of Cu (Figure S31). We note that the improved synthesis of $Cu_3(HITP)_2$ leads to pure Cu(II) samples, in contrast with previous reports where mixed valence contributions to the conductivity could not be ruled out.[12] XPS N 1s spectra of $M_3(HITP)_2$ can be deconvoluted into two peaks at 399.6 and 397.9 eV, which are attributed to the anilinic amine (—NH—) and the quinoid imine (=N—),[32,33] and correlate well with the proposed partial oxidation of HATP to form HITP (Figure S29). The resulting charge neutrality of the frameworks is demonstrated by the absence of possible additional charge-balancing ions (e.g., Na^+ and OAc^-; Figures S32 and S33).

The X-ray absorption near-edge structure (XANES) analysis of $Co_3(HITP)_2$ revealed a pre-edge feature at 7.7092 keV and an edge energy of 7.7204 keV, well-matched with the value expected for Co^{2+} (Figure S34). The weak pre-edge feature at 8.9712 keV in the XANES spectrum of $Cu_3(HITP)_2$ (Figure S37) is characteristic of Cu^{2+}, which has been unambiguously assigned to a 1s → 3d transition. This transition is not observed in Cu^+ with fully occupied 3d orbitals.[34–36] The XANES spectra of $M_3(HITP)_2$ and corresponding model complexes MPc (Pc = phthalocyanine) exhibit similar features, indicating that they have a similar square–planar coordination environment (Figures S34–S37). The fit for the extended X-ray absorption fine structure (EXAFS) spectrum of $Co_3(HITP)_2$ demonstrates the square–planar coordination mode of Co with four Co—N bonds (with a fitted coordination number of 3.9, Table S6) of 1.84 Å (Figure S35), matching well with the structure modeled from PXRD data. The simulated Co—N bond length is also comparable to the 1.824(5) Å averaged Co—N bond length of the Co(II)(s-bqdi)$_2$ complex (s-bqdi = semi-*o*-benzoquinonediimine).[37] Importantly, the +2 oxidation states and square–planar coordination environment of the metal ions are conserved in all $(M_xM'_{3-x})(HITP)_2$ alloys, as verified by XPS (section S16).

X-band electron paramagnetic resonance (EPR) spectroscopy confirmed the presence of HITP-centered organic radicals with g = 2.00. Peaks at g = 5.64 and ~1.9 in the EPR spectrum of $Co_3(HITP)_2$ are typical for high-spin Co^{2+} ions.[38] Similarly, g peaks at 2.17 and 2.02 observed for $Cu_3(HITP)_2$ are typical for square–planar Cu^{2+} ions.[39] Expectedly for non-Kramers Ni^{2+} ions, the X-band EPR spectrum of $Ni_3(HITP)_2$ exhibits only the signal for the ligand-based radical (Figure S42).

Optical spectroscopy provided additional insight into the electronic structures of $(M_xM'_{3-x})(HITP)_2$. Diffuse reflectance UV–visible (DR-UV–vis) spectroscopy revealed a clear absorption edge for $Co_3(HITP)_2$, with broader absorption edges in the near-infrared (IR) region for $Ni_3(HITP)_2$ and $Cu_3(HITP)_2$ (Figure 4). The increase of the background IR absorption, generally associated with free-carrier absorption in degenerate or narrow-gap semiconductors,[40] suggests an enhancement of the free-carrier concentration from $Co_3(HITP)_2$ to $Ni_3(HITP)_2$ (Figure 4a). Indeed, diffuse reflectance infrared Fourier transform spectra (DRIFTS) of $(M_x/M'_{3-x})(HITP)_2$ also reveal a continuous increase of the

https://dx.doi.org/10.1021/jacs.0c04458
J. Am. Chem. Soc. 2020, 142, 12367–12373

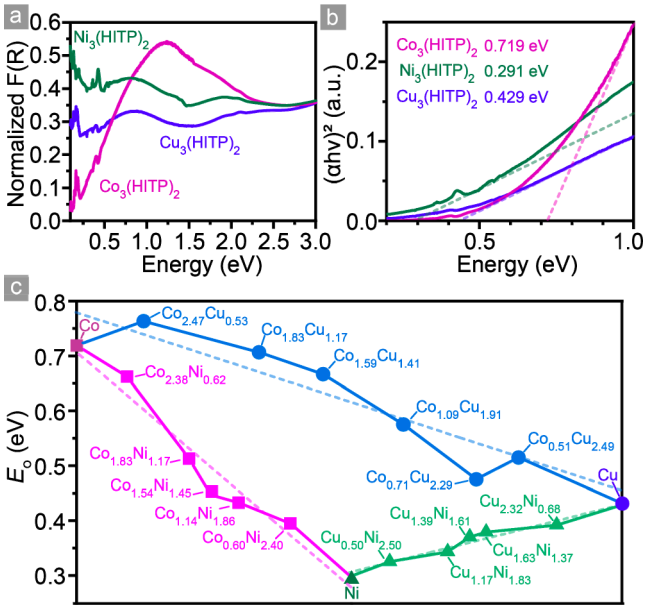

Figure 4. DR-UV−vis and DRIFT spectra of $M_3(HITP)_2$ and $(M_xM'_{3-x})(HITP)_2$. (a) Normalized Kubelka−Munk-transformed spectra of $M_3(HITP)_2$. (b) Normalized Tauc plots from the spectra in (a). Dashed lines indicate best linear fits to the absorption edges. (c) Optical band gaps, E_o, of $(M_xM'_{3-x})(HITP)_2$. Solid lines are guides to the eye; dashed lines are linear fits of E_o.

background absorption with an increasing Cu or Ni content, suggesting the continuous elevation of the free-carrier concentration (Figure S43). Plotting the DR-UV−vis spectra of $M_3(HITP)_2$ in Tauc coordinates[41−43] revealed optical band gaps, E_o, of 0.719, 0.429, and 0.291 eV for $Co_3(HITP)_2$, $Cu_3(HITP)_2$, and $Ni_3(HITP)_2$, respectively. The progressively narrower band gap when transitioning from Co to Cu and Ni is also in agreement with a decreased free carrier concentration for the pure cobalt MOF. Most importantly, DR-UV−vis spectra of $(M_xM'_{3-x})(HITP)_2$ (Figure S43) confirm that the optical band gaps of the alloys can also be continuously tuned over 0.4 eV (cf. Moss−Burstein shift).[41,44] They narrow progressively from 0.662 eV for $(Co_{2.38}Ni_{0.62})(HITP)_2$ to 0.395 eV for $(Co_{0.60}Ni_{2.40})(HITP)_2$ in the CoNi series, from 0.762 eV for $(Co_{2.47}Cu_{0.53})(HITP)_2$ to 0.513 eV for $(Co_{0.52}Cu_{2.48})(HITP)_2$ in the CoCu series, and from 0.392 eV for $(Cu_{2.32}Ni_{0.68})(HITP)_2$ to 0.326 eV for $(Cu_{0.50}Ni_{2.50})$-$(HITP)_2$ in the CuNi series (Figure 4c). Finally, a DRIFTS analysis of $M_3(HITP)_2$ and $(M_xM'_{3-x})(HITP)_2$ showed the expected vibrational bands corresponding to HITP but no features related to electronic transitions below the absorption edges. The influence of defects on optical properties is thus negligible.

The smooth variation in electronic structures derived from optical spectroscopy is also reflected in electrical conductivity measurements for the pure-phase $M_3(HITP)_2$ and the $(M_xM'_{3-x})(HITP)_2$ alloys. Four-contact probe measurements of polycrystalline pellets of $M_3(HITP)_2$ revealed bulk conductivity values, σ, of 0.024, 0.75, and 55.4 S/cm for the pure Co, Cu, and Ni MOFs, respectively, at 296 K. These are higher than the bulk conductivities reported previously for the same compounds,[12,22] which were already among the most conductive MOFs. The metal ions exert an obvious influence on electrical conductivity, at least partially by contributing in different extents to the valence and conduction bands density of states. The electronic nature of the metal ion notwithstanding, we attribute the differences in σ to the slight structural variations among the three materials. In particular, the interlayer displacement, D, and stacking, S, exert an important effect on the transport normal to the sheets. D appears to be optimal in $Ni_3(HITP)_2$ ($D \approx 1.7$ Å in the optimized calculated structure[22]), which also shows the highest bulk conductivity. With D deviating to 1.39(0) Å for $Co_3(HITP)_2$ and 0.86(9) Å for $Cu_3(HITP)_2$, these materials exhibit lower conductivities. Similarly, the higher σ of $Cu_3(HITP)_2$ relative to $Co_3(HITP)_2$ can be traced to its smaller interlayer spacing, 3.16(8) Å, compared to 3.29(8) Å for $Co_3(HITP)_2$.

In line with the spectroscopic and electrical data for the pure phases, the conductivity of $(M_xM'_{3-x})(HITP)_2$ alloys can be tuned precisely for over 4 orders of magnitude from 5.8×10^{-3} S/cm in $(Co_{2.47}Cu_{0.53})(HITP)_2$ to 55.4 S/cm in $Ni_3(HITP)_2$ (Figure 5a). Variations in the electrical conductivity among the

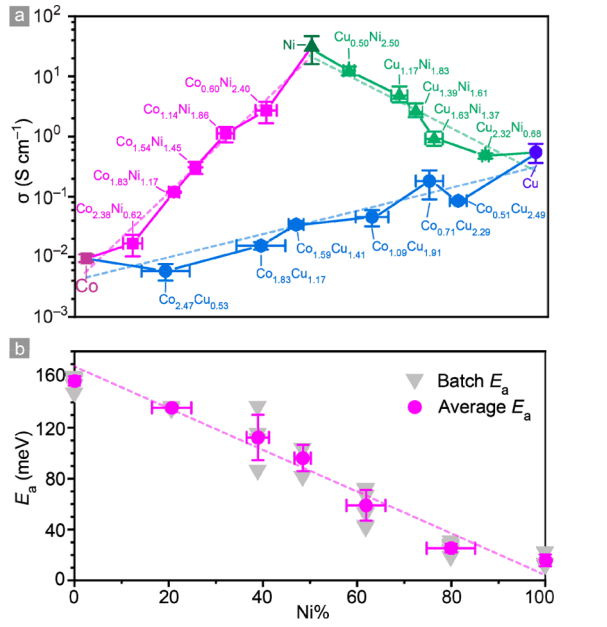

Figure 5. (a) Electrical conductivity data for $(M_xM'_{3-x})(HITP)_2$. Solid lines are guide to the eye; dashed lines are linear fits. (b) Continuous changes of E_a in $(Co_xNi_{3-x})(HITP)_2$. The dashed line is a linear fit with $R^2 = 0.98$.

16 different compositional alloys are in line with all of the discussions above and can be traced to combinations of systematic changes in optical band gaps, free carrier concentrations, and structural parameters, S and D. For instance, increasing the Ni content in the $(Co_xNi_{3-x})(HITP)_2$ series shifts the D and S values in such a way as to enhance interlayer $\pi-\pi$ interactions, which in turn leads to higher σ values. Apparent deviations from these trends, such as with $(Co_{2.47}Cu_{0.53})(HITP)_2$, are also in line with the slightly lower crystallinity for that particular composition, itself likely a result of the relatively more pronounced structural mismatch between $Co_3(HITP)_2$ and $Cu_3(HITP)_2$ (Table S1 and Figure S26).

Notably, control measurements of mechanically blended mixtures of pure-phase $M_3(HITP)_2$ samples behave differently than the alloyed phases, with the more abundant sample dominating the transport in a nonlinear fashion. For instance, mixtures of $Co_3(HITP)_2$ and $Ni_3(HITP)_2$ are nearly as

https://dx.doi.org/10.1021/jacs.0c04458
J. Am. Chem. Soc. 2020, 142, 12367−12373

conductive as the former when the Ni % is low and jump to a conductivity closer to that of the latter when the Ni % reaches 40%. Surprisingly, all blended $Co_3(HITP)_2$:$Cu_3(HITP)_2$ mixtures exhibit lower σ values than $Co_3(HITP)_2$, likely a consequence of the work function/energy level mismatch between individual particles of the two pure phases, which increases the grain boundary resistance (Figure S43).

Variable-temperature (VT) conductivity measurements, performed for the pure phases and for $(Co_xNi_{3-x})(HITP)_2$ as a representative example of the alloyed samples, revealed a temperature-activated bulk transport from 200 to 350 K in all cases (Figure S44). The corresponding activation energies for transport, E_a, correlate well with the σ values: 157 meV for $Co_3(HITP)_2$, 65.3 meV for $Cu_3(HITP)_2$, and 15.7 meV for $Ni_3(HITP)_2$. E_a values for $(Co_xNi_{3-x})(HITP)_2$ alloys vary linearly with the Ni content (Figure 5b), decreasing from 136 meV for $(Co_{2.38}Ni_{0.62})(HITP)_2$ to 25.4 meV for $(Co_{0.60}Ni_{2.40})$-$(HITP)_2$, providing a final confirmation of continuous compositional band engineering through metal substitution.

CONCLUSIONS

A considerable need exists for the improved synthesis of conductive MOFs. Here, synthetic improvements in the production of pure-phase $M_3(HITP)_2$ (M = Co, Ni, Cu) led to more crystalline and porous materials with higher conductivity values than previously reported. These advances also enable a systematic investigation into the influence of the metal ion on physical properties in $(M_xM'_{3-x})(HITP)_2$ alloys, which allow continuous tuning of optical and electronic band gaps and precise modulation of electrical conductivity of over 4 orders of magnitude. These results highlight the importance of synthetic advances for a deeper understanding of structure–function relationships that are crucial for further material developments in this field.

ASSOCIATED CONTENT

Supporting Information

The Supporting Information is available free of charge at https://pubs.acs.org/doi/10.1021/jacs.0c04458.

Additional experimental details and characterization data (PDF)

AUTHOR INFORMATION

Corresponding Author

Mircea Dincă − *Department of Chemistry, Massachusetts Institute of Technology, Cambridge, Massachusetts 02139, United States;* orcid.org/0000-0002-1262-1264; Email: mdinca@mit.edu

Authors

Tianyang Chen − *Department of Chemistry, Massachusetts Institute of Technology, Cambridge, Massachusetts 02139, United States;* orcid.org/0000-0003-3142-8176

Jin-Hu Dou − *Department of Chemistry, Massachusetts Institute of Technology, Cambridge, Massachusetts 02139, United States;* orcid.org/0000-0002-6920-9051

Luming Yang − *Department of Chemistry, Massachusetts Institute of Technology, Cambridge, Massachusetts 02139, United States*

Chenyue Sun − *Department of Chemistry, Massachusetts Institute of Technology, Cambridge, Massachusetts 02139, United States*

Nicole J. Libretto − *Davidson School of Chemical Engineering, Purdue University, West Lafayette, Indiana 47907, United States*

Grigorii Skorupskii − *Department of Chemistry, Massachusetts Institute of Technology, Cambridge, Massachusetts 02139, United States*

Jeffrey T. Miller − *Davidson School of Chemical Engineering, Purdue University, West Lafayette, Indiana 47907, United States;* orcid.org/0000-0002-6269-0620

Complete contact information is available at: https://pubs.acs.org/10.1021/jacs.0c04458

Notes

The authors declare no competing financial interest.

ACKNOWLEDGMENTS

This work was supported by the Army Research Office (Award No. W911NF-17-1-0174). Part of this work (SEM, part of XPS, and HAADF-STEM) made use of the MRSEC Shared Experimental Facilities at MIT, supported by the National Science Foundation under Award No. DMR-1419807. We thank Dr. Yong Zhang for their assistance with HAADF-STEM. This research used resources (aberration-corrected TEM) of the Center for Functional Nanomaterials, which is a US Department of Energy Office of Science Facility, at Brookhaven National Laboratory under Contract No. DE-SC0012704. Use of the Advanced Photon Source at Argonne National Laboratory was supported by the US Department of Energy, Office of Science, Office of Basic Energy Sciences, under Contract No. DE-AC02-06CH11357. Raman spectroscopy and part of XPS were performed at the Harvard Center for Nanoscale Systems (CNS), a member of the National Nanotechnology Infrastructure Network (NNIN), which is supported by the National Science Foundation under Award No. ECS-0335765.

REFERENCES

(1) Sun, L.; Campbell, M. G.; Dincă, M. Electrically Conductive Porous Metal–Organic Frameworks. *Angew. Chem., Int. Ed.* **2016**, *55*, 3566–3579.

(2) (a) Xie, L. S.; Skorupskii, G.; Dincă, M. Electrically Conductive Metal–Organic Frameworks. *Chem. Rev.* **2020**, *120*. (b) Guo, L.; Sun, J.; Wei, J.; Liu, Y.; Hou, L.; Yuan, C. Conductive Metal–Organic Frameworks: Recent Advances in Electrochemical Energy-related Applications and Perspectives. *Carbon Energy* **2020**, *2*, 203.

(3) Sheberla, D.; Bachman, J. C.; Elias, J. S.; Sun, C.-J.; Shao-Horn, Y.; Dincă, M. Conductive MOF Electrodes for Stable Supercapacitors with High Areal Capacitance. *Nat. Mater.* **2017**, *16*, 220–224.

(4) Park, J.; Lee, M.; Feng, D.; Huang, Z.; Hinckley, A. C.; Yakovenko, A.; Zou, X.; Cui, Y.; Bao, Z. Stabilization of Hexaaminobenzene in a 2D Conductive Metal–Organic Framework for High Power Sodium Storage. *J. Am. Chem. Soc.* **2018**, *140*, 10315–10323.

(5) (a) Feng, D.; Lei, T.; Lukatskaya, M. R.; Park, J.; Huang, Z.; Lee, M.; Shaw, L.; Chen, S.; Yakovenko, A. A.; Kulkarni, A.; Xiao, J.; Fredrickson, K.; Tok, J. B.; Zou, X.; Cui, Y.; Bao, Z. Robust and Conductive Two–Dimensional Metal–Organic Frameworks with Exceptionally High Volumetric and Areal Capacitance. *Nat. Energy* **2018**, *3*, 30–36. (b) Sun, J.; Guo, L.; Sun, X.; Zhang, J.; Liu, Y.; Hou, L.; Yuan, C. Conductive Co-based Metal–Organic Framework Nanowires: A Competitive High-rate Anode Towards Advanced Li-ion Capacitors. *J. Mater. Chem. A* **2019**, *7*, 24788–24791.

(6) Shinde, S. S.; Lee, C. H.; Jung, J.-Y.; Wagh, N. K.; Kim, S.-H.; Kim, D.-H.; Lin, C.; Lee, S. U.; Lee, J.-H. Unveiling Dual-Linkage 3D Hexaiminobenzene Metal–Organic Frameworks towards Long–

Lasting Advanced Reversible Zn-Air Batteries. *Energy Environ. Sci.* **2019**, *12*, 727−738.
(7) Clough, A. J.; Yoo, J. W.; Mecklenburg, M. H.; Marinescu, S. C. Two-Dimensional Metal−Organic Surfaces for Efficient Hydrogen Evolution from Water. *J. Am. Chem. Soc.* **2015**, *137*, 118−121.
(8) Miner, E. M.; Fukushima, T.; Sheberla, D.; Sun, L.; Surendranath, Y.; Dincă, M. Electrochemical Oxygen Reduction Catalysed by Ni_3(Hexaiminotriphenylene)$_2$. *Nat. Commun.* **2016**, *7*, 10942.
(9) Dong, R.; Zheng, Z.; Tranca, D. C.; Zhang, J.; Chandrasekhar, N.; Liu, S.; Zhuang, X.; Seifert, G.; Feng, X. Immobilizing Molecular Metal Dithiolene−Diamine Complexes on 2D Metal−Organic Frameworks for Electrocatalytic H_2 Production. *Chem. −Eur. J.* **2017**, *23*, 2255−2260.
(10) Downes, C. A.; Clough, A. J.; Chen, K.; Yoo, J. W.; Marinescu, S. C. Evaluation of the H_2 Evolving Activity of Benzenehexathiolate Coordination Frameworks and the Effect of Film Thickness on H_2 Production. *ACS Appl. Mater. Interfaces* **2018**, *10*, 1719−1727.
(11) Miner, E. M.; Wang, L.; Dincă, M. Modular O_2 Electroreduction Activity in Triphenylene−Based Metal−Organic Frameworks. *Chem. Sci.* **2018**, *9*, 6286−6291.
(12) Campbell, M. G.; Sheberla, D.; Liu, S. F.; Swager, T. M.; Dincă, M. Cu_3(Hexaiminotriphenylene)$_2$: An Electrically Conductive 2D Metal−Organic Framework for Chemiresistive Sensing. *Angew. Chem., Int. Ed.* **2015**, *54*, 4349−4352.
(13) Campbell, M. G.; Liu, S. F.; Swager, T. M.; Dincă, M. Chemiresistive Sensor Arrays from Conductive 2D Metal−Organic Frameworks. *J. Am. Chem. Soc.* **2015**, *137*, 13780−13783.
(14) Smith, M. K.; Mirica, K. A. Self−Organized Frameworks on Textiles (SOFT): Conductive Fabrics for Simultaneous Sensing, Capture, and Filtration of Gases. *J. Am. Chem. Soc.* **2017**, *139*, 16759−16767.
(15) Rubio-Gimenez, V.; Almora-Barrios, N.; Escorcia-Ariza, G.; Galbiati, M.; Sessolo, M.; Tatay, S.; Marti-Gastaldo, C. Origin of the Chemiresistive Response of Ultrathin Films of Conductive Metal−Organic Frameworks. *Angew. Chem., Int. Ed.* **2018**, *57*, 15086−15090.
(16) Meng, Z.; Aykanat, A.; Mirica, K. A. Welding Metallophthalocyanines into Bimetallic Molecular Meshes for Ultrasensitive, Low−Power Chemiresistive Detection of Gases. *J. Am. Chem. Soc.* **2019**, *141*, 2046−2053.
(17) Aubrey, M. L.; Kapelewski, M. T.; Melville, J. F.; Oktawiec, J.; Presti, D.; Gagliardi, L.; Long, J. R. Chemiresistive Detection of Gaseous Hydrocarbons and Interrogation of Charge Transport in Cu[Ni(2,3-Pyrazinedithiolate)$_2$] by Gas Adsorption. *J. Am. Chem. Soc.* **2019**, *141*, 5005−5013.
(18) Sun, L.; Liao, B.; Sheberla, D.; Kraemer, D.; Zhou, J.; Stach, E. A.; Zakharov, D.; Stavila, V.; Talin, A. A.; Ge, Y.; Allendorf, M. D.; Chen, G.; Léonard, F.; Dincă, M. A Microporous and Naturally Nanostructured Thermoelectric Metal−Organic Framework with Ultralow Thermal Conductivity. *Joule* **2017**, *1*, 168−177.
(19) Erickson, K. J.; Léonard, F.; Stavila, V.; Foster, M. E.; Spataru, C. D.; Jones, R. E.; Foley, B. M.; Hopkins, P. E.; Allendorf, M. D.; Talin, A. A. Thin Film Thermoelectric Metal−Organic Framework with High Seebeck Coefficient and Low Thermal Conductivity. *Adv. Mater.* **2015**, *27*, 3453−3459.
(20) Xie, L. S.; Sun, L.; Wan, R.; Park, S. S.; DeGayner, J. A.; Hendon, C. H.; Dincă, M. Tunable Mixed-Valence Doping Toward Record Electrical Conductivity in a Three-Dimensional Metal−Organic Framework. *J. Am. Chem. Soc.* **2018**, *140*, 7411−7414.
(21) Talin, A. A.; Centrone, A.; Ford, A. C.; Foster, M. E.; Stavila, V.; Haney, P.; Kinney, R. A.; Szalai, V.; El Gabaly, F.; Yoon, H. P.; Léonard, F.; Allendorf, M. D. Tunable Electrical Conductivity in Metal−Organic Framework Thin−Film Devices. *Science* **2014**, *343*, 66−69.
(22) Sheberla, D.; Sun, L.; Blood-Forsythe, M. A.; Er, S.; Wade, C. R.; Brozek, C. K.; Aspuru-Guzik, A.; Dincă, M. High Electrical Condutivity in Ni_3(2,3,6,7,10,11-Hexaiminotriphenylene)$_2$, a Semiconducting Metal−Organic Graphene Analogue. *J. Am. Chem. Soc.* **2014**, *136*, 8859−8862.
(23) Van Vleet, M. J.; Weng, T.; Li, X.; Schmidt, J. R. In Situ, Time−Resolved, and Mechanistic Studies of Metal−Organic Framework Nucleation and Growth. *Chem. Rev.* **2018**, *118*, 3681−3721.
(24) Marcus, Y. The Effectivity of Solvents as Electron Pair Donors. *J. Solution Chem.* **1984**, *13*, 599−624.
(25) Skorupskii, G.; Trump, B. A.; Kasel, T. W.; Brown, C. M.; Hendon, C. H.; Dincă, M. Efficient and Tunable One−Dimensional Charge Transport in Layered Lanthanide Metal−Organic Frameworks. *Nat. Chem.* **2020**, *12*, 131−136.
(26) Denton, A. R.; Ashcroft, N. W. Vegard's Law. *Phys. Rev. A: At., Mol., Opt. Phys.* **1991**, *43*, 3161−3164.
(27) McIntyre, N. S.; Cook, M. G. X-ray Photoelectron Studies on Some Oxides and Hydroxides of Cobalt, Nickel, and Copper. *Anal. Chem.* **1975**, *47*, 2208−2213.
(28) Moretti, G. Auger Parameter and Wagner Plot in the Characterization of Chemical States by X−ray Photoelectron Spectroscopy: A Review. *J. Electron Spectrosc. Relat. Phenom.* **1998**, *95*, 95−144.
(29) Matienzo, J.; Yin, L. I.; Grim, S. O.; Swartz, W. E., Jr X−ray Photoelectron Spectroscopy of Nickel Compounds. *Inorg. Chem.* **1973**, *12*, 2762−2769.
(30) Frost, D. C.; Ishitani, A.; McDowell, C. A. X−ray Photoelectron Spectroscopy of Copper Compounds. *Mol. Phys.* **1972**, *24*, 861−877.
(31) Yin, L.; Adler, I.; Tsang, T.; Matienzo, L. J.; Grim, S. O. Paramagnetism and Shake−up Satellites in X-ray Photoelectron Spectra. *Chem. Phys. Lett.* **1974**, *24*, 81−84.
(32) Tan, K. L.; Tan, B. T. G.; Kang, E. T.; Neoh, K. G. X−ray Photoelectron Spectroscopy Studies of the Chemical Structure of Polyaniline. *Phys. Rev. B: Condens. Matter Mater. Phys.* **1989**, *39*, 8070−8073.
(33) Mohtasebi, A.; Chowdhury, T.; Hsu, L. H.; Biesinger, M. C.; Kruse, P. Interfacial Charge Transfer Between Phenyl−capped Aniline Tetramer Films and Iron Oxide Surfaces. *J. Phys. Chem. C* **2016**, *120*, 29248−29263.
(34) Bair, R. A.; Goddard, W. A., III *Ab initio* Studies of the X−ray Absorption Edge in Copper Complexes. I. Atomic Cu^{2+} and Cu(II)Cl_2. *Phys. Rev. B: Condens. Matter Mater. Phys.* **1980**, *22*, 2767−2776.
(35) Sano, M.; Komorita, S.; Yamatera, H. XANES Spectra of Copper (II) Complexes: Correlation of the Intensity of the 1s → 3d Transition and the Shape of the Complex. *Inorg. Chem.* **1992**, *31*, 459−463.
(36) Chaboy, J.; Muñoz-Páez, A.; Carrera, F.; Merkling, P.; Marcos, E. S. *Ab initio* X-ray Absorption Study of Copper K−edge XANES Spectra in Cu(II) Compounds. *Phys. Rev. B: Condens. Matter Mater. Phys.* **2005**, *71*, 134208.
(37) Peng, S.-M.; Chen, C.-T.; Liaw, D.-S.; Chen, C.-I.; Wang, Y. Establishment of the Bond Patterns of *o*-Benzoquinonediimine and Semi-*o*-Benzoquinonediimine: Crystal Structures of Metal Complexes, $[Fe^{II}(bqdi)_3](PF_6)_2$,$[Co^{II}(s\text{-}bqdi)_2]$ and $[Co^{III}Cl(s\text{-}bqdi)_2)]$. *Inorg. Chim. Acta* **1985**, *101*, L31−L33.
(38) Jiménez, H. R.; Salgado, J.; Moratal, J. M.; Morgenstern-Badarau, I. EPR and Magnetic Susceptibility Studies of Cobalt (II)- and Nickel (II)-substituted Azurins from Pseudomonas Aeruginosa. Electronic Structure of the Active Sites. *Inorg. Chem.* **1996**, *35*, 2737−2741.
(39) Garribba, E.; Micera, G. The Determination of the Geometry of Cu (II) Complexes: An EPR Spectroscopy Experiment. *J. Chem. Educ.* **2006**, *83*, 1229−1232.
(40) Amalric Popescu, D.; Herrmann, J.-M.; Ensuque, A.; Bozon-Verduraz, F. Nanosized Tin Dioxide: Spectroscopic (UV-Vis, NIR, EPR) and Electrical Conductivity Studies. *Phys. Chem. Chem. Phys.* **2001**, *3*, 2522−2530.
(41) Chu, J.; Sher, A. *Physics and Properties of Narrow Gap Semiconductors*; Springer: New York, NY, 2008.
(42) Nowak, M.; Kauch, B.; Szperlich, P. Determination of Energy Band Gap of Nanocrystalline SbSI Using Diffuse Reflectance Spectroscopy. *Rev. Sci. Instrum.* **2009**, *80*, No. 046107.

(43) Gibbs, Z. M.; LaLonde, A.; Snyder, G. J. Optical Band Gap and the Burstein-Moss Effect in Iodine Doped PbTe Using Diffuse Reflectance Infrared Fourier Transform Spectroscopy. *New J. Phys.* **2013**, *15*, No. 075020.
(44) Kudman, I.; Seidel, T. Absorption Edge in Degenerate p−Type GaAs. *J. Appl. Phys.* **1962**, *33*, 771−773.

https://dx.doi.org/10.1021/jacs.0c04458
J. Am. Chem. Soc. 2020, 142, 12367−12373